



# Influence of lattice strain on Er<sup>3+</sup> ions activated magnesium zirconium phosphate phosphors: Morphological, structural, and photoluminescence properties

Tribikram Choudhury, Eric Kumi-Barimah<sup>\*</sup>, Padmaja Parameswaran Nampi, Girish M. Kale, Gin Jose

School of Chemical and Process Engineering, University of Leeds, Leeds LS2 9JT, UK

## ARTICLE INFO

### Keywords:

Synthesis  
Magnesium zirconium phosphate  
Nanophosphors  
Erbium  
Lattice strain  
Photoluminescence

## ABSTRACT

Rare earth ions doped alkaline metal zirconium phosphors have recently received significant attention in several applications including light-emitting diodes (LEDs) based solid-state lighting, solar panels, barcode readers and fluorescent labels focusing on the ultraviolet (UV) to visible (Vis) spectrum photoluminescence (PL) properties. Near-infrared (NIR) PL properties of rare earth ions doped magnesium zirconium phosphate (MZP) nanophosphors characteristics have not been investigated and considered as good candidates for optical amplifier and photonics applications. In this study, erbium doped magnesium zirconium phosphate (Er<sup>3+</sup>-doped MgZr<sub>4</sub>(PO<sub>4</sub>)<sub>6</sub>) nanophosphors containing 0.0, 0.25, 0.5, 0.75 and 1.0 mol% Er<sup>3+</sup> were synthesised using a sol-gel technique. The samples prepared were calcined at 900 °C. Nanopowders of the samples were examined by the transmission electron microscopy (TEM), X-ray diffraction (XRD), and Raman spectroscopy to determine the surface morphology, particle size, crystallographic phase, crystalline structure, and lattice strain. Increasing in the Er<sup>3+</sup>-ion concentrations do not have significant influence on the crystallite size, with an average crystallite size range from ~ 28 nm to 32 nm. However, the lattice strain parameter of the Er<sup>3+</sup> doped MZP samples decreased slightly as compared to the pure undoped MgZr<sub>4</sub>(PO<sub>4</sub>)<sub>6</sub>. The Er<sup>3+</sup> dopant was found to influence the photoluminescence properties measured at room temperature under a 980 nm excitation source. Systematic analysis revealed the presence of broad emission band corresponding to the <sup>4</sup>I<sub>13/2</sub> → <sup>4</sup>I<sub>15/2</sub> transition. The results showed that 0.5 mol % Er<sup>3+</sup> doped sample exhibits a full width half maximum (FWHM) value of 38 nm with a long photoluminescence lifetime of 5.47 ms. The results obtained clearly demonstrates that 0.5 mol% Er<sup>3+</sup> doped MgZr<sub>4</sub>(PO<sub>4</sub>)<sub>6</sub> nanophosphors has a huge potential for integrated photonic applications such as lighting, biosensing, compact waveguide amplifiers, and lasers with emission properties in the IR region.

## 1. Introduction

In recent years, several inorganic nanophosphor materials have been investigated extensively as host materials for luminescent rare earth ions and becoming attractive for photonic devices such as light-emitting diodes, solar panels, biosensors, quantum storage, and fibre optic communication [1,2,3,4]. The unique lattice strain and crystallite-size dependency on the crystal structure and morphology of rare earth doped inorganic nanophosphors with superior optical properties play significant role in some of the aforementioned applications mentioned above. Among these, alkali metal (M = Na, K) zirconium orthophosphate (MZr<sub>4</sub>(PO<sub>4</sub>)<sub>6</sub>) phosphors have a great potential in practical

applications owing to their superior physical, chemical and optical properties [5,6,7]. For instance, ZrP<sub>2</sub>O<sub>7</sub> has a refractive index ranging from 1.54 to 1.66 at 633 nm and at room temperature and, high transmittance at the visible, near infrared (NIR) regions [8,9]. However, application of most of these inorganic nanophosphors have been focused on light emitting diodes to produce colours in a spectral range of 400–800 nm or for white generation by integrating with rare earth ions such as Eu<sup>3+</sup>, Dy<sup>3+</sup> and Tb<sup>3+</sup> [10,11,12]. The light-emitting diode of different colours have been realised using either their down conversion or upconversion to enable the rare earth ions/transition metals doped phosphors converting ultra-violet or infrared light sources to blue, green and red or white photoluminescence emissions. However, it should be

<sup>\*</sup> Corresponding author.

E-mail address: [e.kumi-barimah@leeds.ac.uk](mailto:e.kumi-barimah@leeds.ac.uk) (E. Kumi-Barimah).

<https://doi.org/10.1016/j.mseb.2021.115582>

Received 18 March 2021; Received in revised form 23 October 2021; Accepted 13 December 2021

Available online 23 December 2021

0921-5107/© 2022 The Authors. Published by Elsevier B.V. This is an open access article under the CC BY license (<http://creativecommons.org/licenses/by/4.0/>).

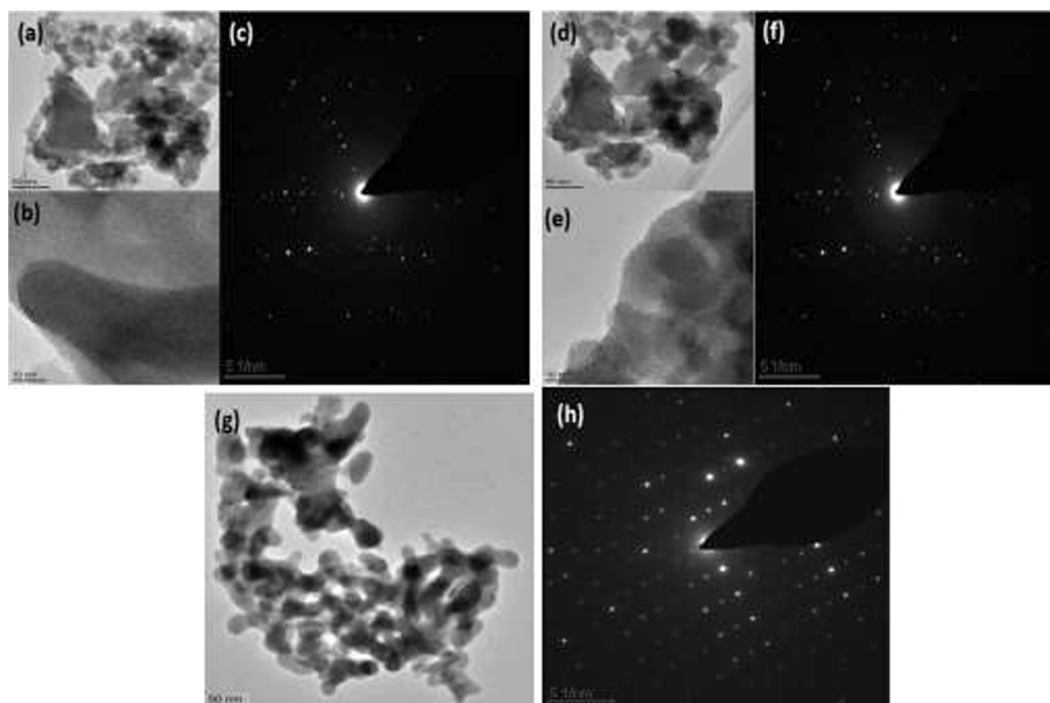


**Fig. 1.** TEM images represent different concentrations of  $\text{Er}^{3+}$  ion doped MZP nanopowder phosphors calcined at  $900\text{ }^\circ\text{C}$  for 3 h with SAED patterns: (a–c) MZP0, (d–f) MZP1 and (g–h) MZP4.

noted that the alkali metal zirconium orthophosphates are likely to be naturally sensitive to moisture and therefore be unstable in ambient conditions for extended length of time.

Choice of appropriate host material is highly crucial in the effective doping and hence modulating the material for ultimate advanced applications. Among various host lattices, magnesium zirconium orthophosphate (MZP) nanopowder having a NASICON type crystal structure has been found to be an appropriate host material for rare earth ions as well as for application as microwave dielectric materials [14,15] and as solid electrolyte in high temperature electrochemical sensor in non-ferrous scrap metal refining and virgin metal alloying operations [16,17,18]. This host crystal is also suitable for exploiting photoluminescence properties of the  $\text{Er}^{3+}$  ion dopant due to its properties such as a high phonon energy of  $1030\text{ cm}^{-1}$ , high refractive index ( $\text{MgO} = 1.735$ ,  $\text{ZrO}_2 = 2.180\text{--}2.670$ , and  $\text{PO}_4 = 1.603$ ), high transmittance at visible-NIR wavelength, and thermal stability [13]. MZP doped with luminescent rare earth such as  $\text{Er}^{3+}$  ions would be suitable material as a result of an intrinsically faster photoluminescence emission for numerous applications including a scintillator, light emitting diodes, photocatalyst, and biosensing in the visible-NIR wavelength region (400 to 800 nm). Additionally, it has potential for the formation of hybrid-composite waveguide amplifiers and compact lasers at NIR emission around  $1.53\text{ }\mu\text{m}$ . The MZP phosphor as a host would enable incorporation of a high rare earth ions concentration and solubility along with weak ion-ion interactions to minimise PL and lifetime quenching. Over the years, several methods have been reported for synthesising undoped and rare-earth ions doped alkali metal zirconium phosphate, which include co-precipitation method, solid-state reaction, sol-gel and combustion [4,13,14,15,16]. Adamu et al. [14] synthesised  $\text{MgZr}_4(\text{PO}_4)_6$  nanopowders using novel and economical sol-gel method at a reduced temperature to investigate the calcination process, and possible phase transformation due to its potential application as a solid state electrochemical sensor in non-ferrous scrap metal refining. Similarly, Li et al. [18] employed solid state reaction technique to fabricate different concentration of  $\text{Ce}^{3+}$  doped  $\text{MgZr}_4(\text{PO}_4)_6$  to study phase and microstructure, conductivity and dielectric properties. Recently, Nataliia et al. [13] prepared NASICON-like ion conductive rhombohedral rare

earth elements doped lithium zirconium phosphate utilising two different synthesis approaches including polymerizable-complex Pechini method and a solid state reaction. They examined the crystal structure and characteristics of their colour optical properties in the visible spectrum (400 to 700 nm) for pigment application. In addition, nano-structured mesoporous sodium zirconium phosphate was fabricated and characterised for separation and extraction of uranyl ions from real samples [19,20]. Furthermore,  $\text{Eu}^{2+}$  doped  $\text{A}_{0.5}\text{Zr}_2(\text{PO}_4)_3$  ( $\text{A} = \text{Ca}, \text{Sr}, \text{Ba}$ ) phosphors were synthesized by a co-precipitation method [16]. Their visible spectrum photoluminescent spectroscopy and structural properties were explored. Most of the previous research on undoped and rare earth ions doped alkali metal zirconium phosphate nanopowders focussed on structural and visible luminescent properties without any report on near-infrared luminescent properties studies around  $1530\text{ nm}$ . Among these methods, sol-gel synthesis technique has become attractive owing to its advantage over the other techniques since it is environmentally friendly, less energy intensive and yields fine powders easy to compact and sinter at lower temperatures to nearly full density [9]. Furthermore, sol-gel process can circumvent high volatility of phosphorus above  $1200\text{ }^\circ\text{C}$ , which leads to decomposition of MZP into numerous undesired polymorphic phases such as  $\text{ZrO}_2$ ,  $\text{ZrP}_2\text{O}_7$  and  $\text{Zr}_2\text{O}(\text{PO}_4)_2$  [10,11]. In addition, the process allows formation of homogeneous nanostructures with high surface area-to-volume ratio, which enhances the photoluminescence properties at the NIR.

To the best of our knowledge, this is the first report of MZP nanopowders doped with different concentration of  $\text{Er}^{3+}$  ions prepared by novel and economical sol-gel method. The X-ray line profile analysis was performed to understand the effect of peak broadening on lattice strains and crystallite sizes by utilising Williamson-Hall method and Scherrer's equation. Furthermore, structural analysis of the nanopowders was carried out by Raman spectroscopy. In addition, the influence of lattice strains on the NIR PL emission and lifetime at  $1533\text{ nm}$  ( ${}^4\text{I}_{13/2} \rightarrow {}^4\text{I}_{15/2}$  transition) of the MZP incorporated with different concentrations of  $\text{Er}^{3+}$  ions were also investigated, respectively.

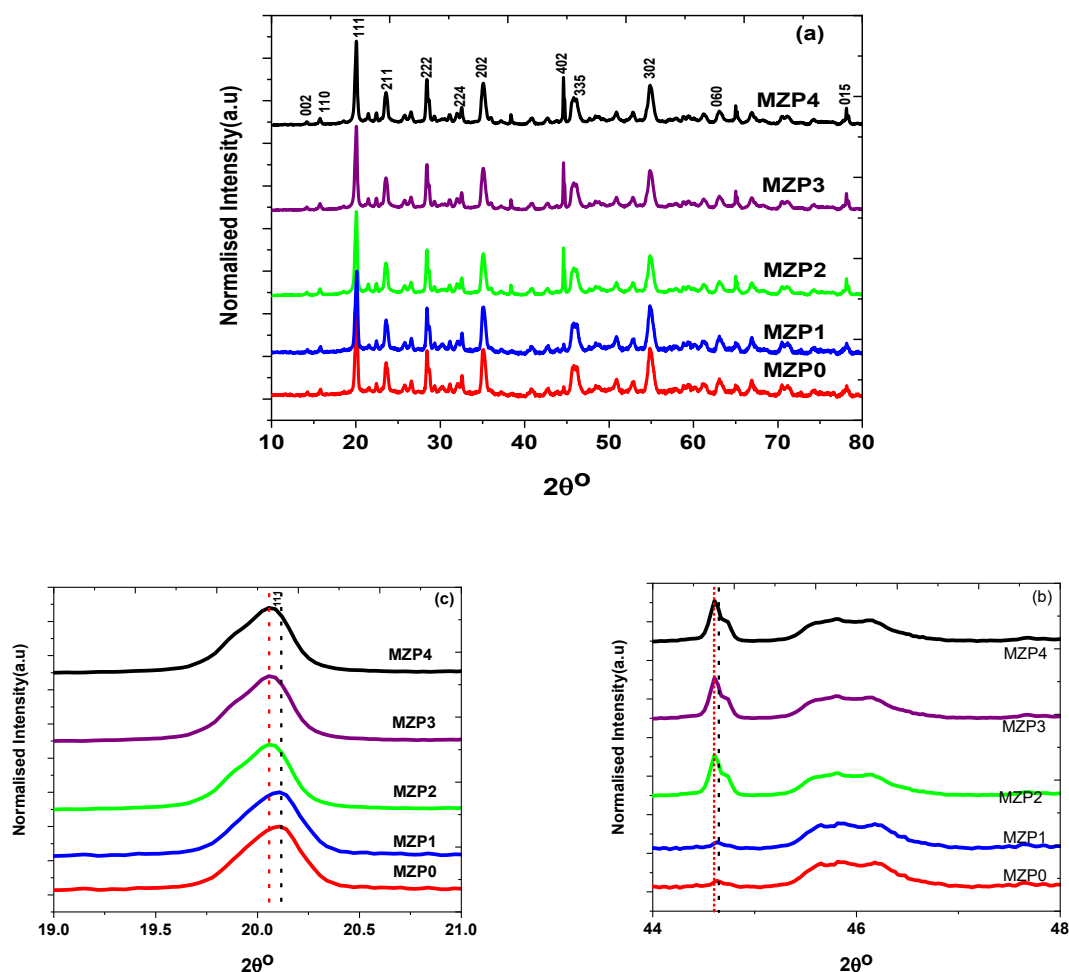


Fig. 2. (a) XRD patterns of MZP0 and  $\text{Er}^{3+}$  doped MZP (MZP1, MZP2, MZP3 and MZP4) calcined at 900 °C for 3 h, Diffraction patterns within  $2\theta$  range from (b) 19 to 21°, (c) 44 to 48°

## 2. Experimental technique

The raw materials for nanophosphor synthesis consisted of magnesium nitrate hexahydrate ( $\text{MgN}_2\text{O}_6 \cdot 6\text{H}_2\text{O}$ , 99.99% purity), ammonium dihydrogen phosphate ( $\text{NH}_4\text{H}_2\text{PO}_4$ , 99.999% purity), zirconyl chloride octahydrate ( $\text{ZrOCl}_2 \cdot 8\text{H}_2\text{O}$ , 99.99% purity), and erbium nitrate pentahydrate ( $\text{Er}(\text{NO}_3)_3 \cdot 5\text{H}_2\text{O}$ , 99.9% purity), which were all purchased from Sigma-Aldrich, UK and used without any further purification.  $\text{Er}^{3+}$  doped MZP phosphors were synthesised with molar compositions of (9.09-X) mol% of  $\text{MgN}_2\text{O}_6 \cdot 6\text{H}_2\text{O}$ , 54.55 mol% of  $\text{NH}_4\text{H}_2\text{PO}_4$ , 36.36 mol% of  $\text{ZrOCl}_2 \cdot 8\text{H}_2\text{O}$  and  $x$  mol% of  $\text{Er}(\text{NO}_3)_3 \cdot 5\text{H}_2\text{O}$  ( $x = 0.00, 0.25, 0.50, 0.75$  and  $1.00$  mol%) denoted as MZP0, MZP1, MZP2, MZP3, and MZP4 by using a modified sol-gel technique [14]. In brief, appropriate amounts of  $\text{MgN}_2\text{O}_6 \cdot 6\text{H}_2\text{O}$ ,  $\text{NH}_4\text{H}_2\text{PO}_4$ , and  $\text{Er}(\text{NO}_3)_3 \cdot 5\text{H}_2\text{O}$  were initially weighed and then mixed with 150 mL deionised water in 3 different beakers. The precursor solutions were mixed according to the selected compositions and then continuously stirred in a beaker with a magnetic stirrer to form a clear homogenous solution. This was followed by adding  $\text{ZrOCl}_2 \cdot 8\text{H}_2\text{O}$  aqueous solution in dropwise via syringe. The final precursor solution was allowed to stir for 2 h to yield homogenous sol-gel solution and then dried on a hot plate at 100 °C for 24 h. Lastly, the dried powders were ground with agate mortar and pestle into fine powder and then calcined at 900 °C for 3 h to convert into single phase nanopowders of  $\text{Er}^{3+}$  doped MZP.

The surface morphology along with the selected area electron diffraction (SAED) patterns was determined by the transmission electron microscopy using a FEI Tecnai F20 Transmission Electron Microscope at

an accelerating voltage of 200 kV. The phase purity of the samples was determined using X-ray diffraction (XRD, P'Analytical X'Pert, MPD, Netherlands) with  $\text{CuK}\alpha$  ( $\lambda = 1.5406 \text{ \AA}$ ) radiation. Following this, X'Pert HighScore Plus software was utilised to analyse the XRD data. Renishaw Raman microscope under a 514.5 nm excitation source from a green  $\text{Ar}^+$  laser was also employed to provide molecular structure fingerprints of the nanopowders of Er doped MPZ phosphors from 200 to 3200  $\text{cm}^{-1}$  wavenumber range. The FLS920 fluorescence spectrometer (Edinburgh Instruments, UK) with a semiconductor laser diode emitting at 980 nm was used to measure photoluminescence spectra and lifetimes of the nanopowder phosphors at the NIR (1400–1700 nm).

## 3. Results and discussion

### 3.1. Morphological and structural properties

#### 3.1.1. Transmission electron microscopy studies

The morphology and crystal structures of the undoped MZP and  $\text{Er}^{3+}$ -ions doped MZP nanopowders synthesised were studied by using high-resolution TEM (HR-TEM). The high-resolution TEM images and corresponding selected area electron diffraction (SAED) patterns of MZP0, MZP1 and MZP4 is presented in Fig. 1. Fig. 1(a) illustrates TEM of undoped MZP0 sample, which reveals that the particulates are aggregated. High resolution image and SAED of MZP0 is presented as Fig. 1(b) and (c), respectively. The existence of numerous discrete spots line-up or randomness of the diffraction patterns forming around the central spot in the SAED pattern suggests the undoped MZP0 is crystalline. Thus,

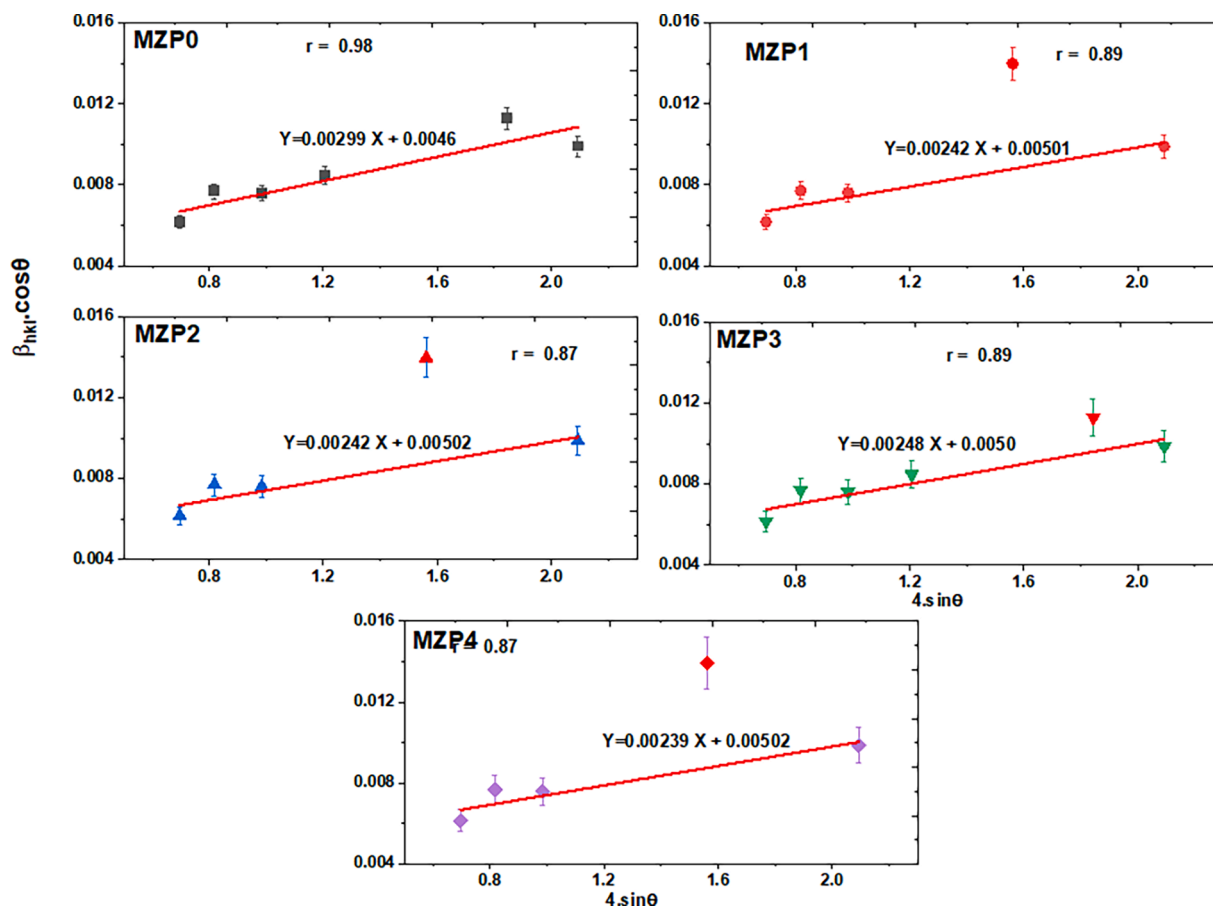


Fig. 3. Williamson-Hall plots of pure  $\text{MgZr}_4(\text{PO}_4)_6$  and different concentrations of Er doped  $\text{MgZr}_4(\text{PO}_4)_6$  with their corresponding equation and correlation of a line.

such crystal formation of sample MZP0 could be attributed to long-ranger order. Subsequently,  $\text{MgZr}_4(\text{PO}_4)_6$  nanophosphors doped with different concentrations of  $\text{Er}^{3+}$  ions as described in the experimental section were studied using TEM. The surface morphology and SAED pattern of the crystal lattice of sample MZP1 are identical to sample MZP0 and depicted in Fig. 1[(d), (e), and (f)] respectively. In contrast, as the  $\text{Er}^{3+}$  ion concentration increases from 0.5 to 1.0 mol% in the steps of 0.25 mol% [MZP2, MZP3 and MZP4] the crystallite sizes appeared to decrease slightly and remain agglomerated. Fig. 1(g) and (h) shows TEM micrograph of sample MZP4 and SAED pattern respectively exhibiting a crystalline nanoparticulate sample represented by the discrete spot with a high degree of order in the crystal lattice and devoid of boundaries. A fine structure in single crystal electron diffraction patterns indicates possible composition-dependent lattice strains and creation of short-range order. In addition, the SAED pattern consists of numerous order reflections in both directions, which suggests a high crystallographic order existing in this crystal. Similarly, the TEM and SAED patterns of samples MZP2 and MZP3 are identical to sample MZP4, which are not shown here.

### 3.1.2. X-ray diffraction measurements

XRD analysis was performed to ascertain phase purity of the undoped and  $\text{Er}^{3+}$  doped  $\text{MgZr}_4(\text{PO}_4)_6$  nanoparticles. Fig. 2(a) shows the XRD patterns of undoped MZP and various  $\text{Er}^{3+}$  doped  $\text{MgZr}_4(\text{PO}_4)_6$  nanophosphors measured within  $2\theta$  scanning range of  $10^\circ$  to  $80^\circ$  at room temperature. The XRD pattern of the undoped sample matches with the standard data of  $\text{MgZr}_4(\text{PO}_4)_6$  available in International Center for Diffraction Data (ICDD) card number of 04-045-0419 with monoclinic crystal structure, space group of  $P_{21/n}$ , and space group number  $I_4$  without any additional impurity phase. This result of MZP0 sample pattern is comparable and consistent with Adamu et al. [14,17], Pet'kov

et al. [21], and Kazakos-kijowski et al. [22] where they synthesised pure  $\text{MgZr}_4(\text{PO}_4)_6$  using sol-gel synthesising method. According to the ICDD data, the pure monoclinic crystal structure has a space group of  $P_{21/n}$  [14,17]. Moreover, the XRD pattern of sample MZP0 has several diffraction peaks at  $2\theta = 20.07, 23.61, 28.50, 32.53, 35.14, 45.96, 54.93$  and  $63.13^\circ$ ; which correspond to reflection from crystallographic planes or Miller index ( $hkl$ ) of (111), (211), (022), (213), (202), (402), (313) and (060). These diffraction peaks matched well with the observed and computer calculated  $2\theta$  values reported elsewhere [26]. Doping the  $\text{MgZr}_4(\text{PO}_4)_6$  with 0.25 mol% of  $\text{Er}^{3+}$  ion concentration, causes negligible difference in the XRD pattern compared to sample MZP0. On the other hand, as the  $\text{Er}^{3+}$  ion concentration increases from 0.50 mol% to 1.00 mol%, new minor diffraction peak at  $2\theta = 44.62^\circ$  [shown in Fig. 2 (b)] tends to increase and broaden. This peak is can be assigned to  $\text{Er}^{3+}$  doped zirconium oxide phosphate ( $\text{Er}:\text{ZrO}(\text{PO}_4)_2$ ) phase. Such variation in the diffraction patterns can contribute to lattice strain in the nanophosphors due to crystal imperfection or  $\text{Er}^{3+}$  displacing  $\text{Mg}^{2+}$  ions in the  $\text{MgZr}_4(\text{PO}_4)_6$  crystal structure. Furthermore, the peak shifting, broadening and increasing intensity of the nanophosphors diffraction peaks occurred at  $2\theta = 20.07^\circ$  and  $44.62^\circ$  [Fig. 2 (b) and (c)] can be ascribed to combine effect of crystal structure variation owing to presence of  $\text{Er}^{3+}$  and other factors including crystallite size, and lattice strain [23,24]. Additionally, these changes in the XRD patterns could be attributed to crystalline transformation from long-range order to short-ranger order.

For instance, it is well known that the crystallite size of a nanopowder less than 100 nm produces broadened diffraction peaks instead of a sharp; while the lattice strain existing in such samples can lead to broadening of Bragg diffraction and increasing intensity peaks. Conversely, instrumental broadening effect was eliminated from these measurements by initially performing XRD of standard silicon powder

**Table 1**

Average crystallite size and lattice strain for pure  $\text{MgZr}_4(\text{PO}_4)_6$  and various concentrations of Er doped  $\text{MgZr}_4(\text{PO}_4)_6$ .

Sample ID	Crystallite size (nm)		Lattice strain ( $\epsilon \times 10^{-3}$ )
	Debye-Scherrer's Eqn.	W-H method	
MZP0	20.73	31.82	2.99
MZP1	20.67	29.21	2.42
MZP2	20.69	29.16	2.40
MZP3	20.70	29.16	2.48
MZP4	20.70	28.15	2.39

under the same experimental condition where we observed the peak width centred at  $\sim 36^\circ$  [not shown here]. Initially, the average crystallite size ( $D_c$ ) of each nanophosphor as-prepared was estimated by using Debye-Scherrer's equation based on peak broadening, which is given below [23,24,25];

$$D_c = \frac{k\lambda}{\beta \cdot \cos\theta} \quad (1)$$

where  $\lambda$  is the wavelength of incident X-ray beam in nanometres ( $\lambda = 0.15406$  nm),  $\beta$  is the full width half maximum of the peak in radians,  $2\theta$  is the scattering Bragg angle in radians, and  $k$  is a constant whose value depends on particle shape (0.95). In addition to the Debye-Scherrer equation, Williamson-Hall (W-H) method was also employed to elevate crystallite size for comparison and lattice strain [23,24,25,26,27].

According to W-H method, the broadening owing to the lattice strain distortion and crystal imperfection can be expressed as [27,28,29,30,25]:

$$B_s = 4\epsilon \cdot \tan\theta \quad (2)$$

where  $B_s$  is the peak broadening because of lattice strain and  $\epsilon$  is the strain distribution inside the crystalline nanopowder. From Eq. (1) and (2), the total peak broadening ( $B_{hkl}$ ) is related to deconvolution of lattice strain and crystallite size equations which can be formulated as.

$$B_{hkl} = \frac{k\lambda}{D} \cdot \frac{1}{\cos\theta} + 4\epsilon \cdot \tan\theta \quad (3)$$

The equation (3) above can be rearranged as follows

$$B_{hkl} \cdot \cos\theta = \frac{k\lambda}{D} + 4\epsilon \cdot \sin\theta \quad (4)$$

Thus, Eq. (4) represents the W-H method. The crystallite size and lattice strain of the MZP samples prepared at different concentrations of  $\text{Er}^{3+}$  ions were determined by plotting  $B_{hkl} \cdot \cos\theta$  as a function of  $4\sin\theta$  (Williamson-Hall plot) as shown in Fig. 3. Crystallite size and lattice strain distribution were calculated by using y-intercept and slope of the straight line of each sample. The diffraction planes relating to (111), (211), (022), (213), (202), (402), (313) and (060) peaks were employed to calculate the crystallite sizes and lattice strain using Eq. (4). Table 1 illustrates comparison of crystallite sizes estimated from Debye-Scherrer's equation and W-H method as well as the lattice strain distribution obtained from W-H method. It is observed that the crystallite size of  $\text{MgZr}_4(\text{PO}_4)_6$  nanopowders are almost identical for each formula, however, the crystallite sizes extracted from W-H method are higher than those obtained from Debye-Scherrer's equation. The variation in crystallite sizes between the two approaches is attributed to the fact that Debye-Scherrer's equation assumes lattice strain part of W-H equation to be zero. Henceforth, the crystallite size is underestimated if only the diffraction peak broadening is taking into account. Also, the lattice strain strongly depends on the  $\text{Er}^{3+}$  ion dopant with an average value of  $\sim 2.42 \times 10^{-3}$ , which is almost identical to the pure/undoped  $\text{MgZr}_4(\text{PO}_4)_6$  phosphor ( $2.99 \times 10^{-3}$ ). According to Nath et al [13], the slight change in lattice strain is ascribed to the lattice expansion in the

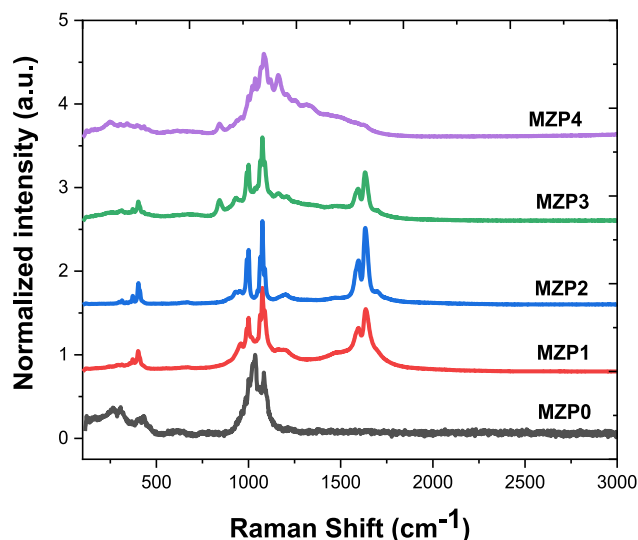


Fig. 4. Raman spectra of undoped and  $\text{Er}^{3+}$  doped  $\text{MgZr}_4(\text{PO}_4)_6$  phosphors.

crystalline nanopowders as a result of size confinement. On the contrary, doping  $\text{MgZr}_4(\text{PO}_4)_6$  with  $\text{Er}^{3+}$  ions could initiate atomic rearrangement thus modifies the size confinement as compared to pure  $\text{MgZr}_4(\text{PO}_4)_6$  and then leads to decrease lattice strain. The lattice strain decreases with increasing  $\text{Er}^{3+}$  concentration in MZP could be due to the lattice relaxation as a result of the formation of oxygen vacancies by  $\text{Er}^{3+}$  ion aliovalent substitution in MZP. In addition, the peak broadening and lattice defect observed in the XRD pattern could generate lattice strain due to large ionic radii of the  $\text{Er}^{3+}$  ions in octahedral coordination (0.89 Å) as compared to cationic radii of  $\text{Mg}^{2+}$  and  $\text{Zr}^{4+}$  in tetrahedral coordination of 0.57 Å and 0.72 Å.

### 3.2. Spectroscopic and photoluminescence properties

#### 3.2.1. Raman spectroscopy

Raman spectroscopic investigation of as-synthesised undoped  $\text{MgZr}_4(\text{PO}_4)_6$  and various concentrations ranging from 0.25 to 1 mol% in the step of 0.25 mol% of Er doped  $\text{MgZr}_4(\text{PO}_4)_6$  nanophosphors were performed under a 514.5 nm excitation laser at room temperature to identify molecular structures; which is presented in Fig. 4. The Raman spectrum of sample MZP0 exhibits a weak vibration band of lattice modes positioned at  $265 \text{ cm}^{-1}$  and another a weak Raman band at  $309 \text{ cm}^{-1}$ , which is consistent with  $\text{Zr-PO}_4$  modes [31]. The two weaker peaks appear at  $430 \text{ cm}^{-1}$  and  $625 \text{ cm}^{-1}$  are assigned to  $\text{PO}_4 V_2$  symmetric and  $V_4$  antisymmetric bending groups deformation vibration [32,33,34,35,36,37]. Furthermore, the weak peak at  $625 \text{ cm}^{-1}$  appears to be overlapping with that of  $602 \text{ cm}^{-1}$  corresponding to the oxygen ion vacancies due to the  $\text{Er}^{3+}$  substitution in MZP0. This correlated well with the decrease in strain with increasing  $\text{Er}^{3+}$  concentration in MZP as shown in Table 1. Besides these vibrational modes, there occurs another well resolved  $\nu_3$  antisymmetric vibration bands from  $868 \text{ cm}^{-1}$  to  $1204 \text{ cm}^{-1}$  with an intense peak at  $1030 \text{ cm}^{-1}$  and a shoulder at  $1080 \text{ cm}^{-1}$  [4,32]. These vibrational bands correspond to the phonons of the orthophosphate ions,  $(\text{PO}_4)^{3-}$ , phosphor host. Additionally, doping  $\text{MgZr}_4(\text{PO}_4)_6$  with  $\text{Er}^{3+}$  ion concentrations ranging from 0.25 mol to 1.00 mol reveal additional vibration modes occurring at 406, 991, 1077, and  $1627 \text{ cm}^{-1}$ , respectively. These vibration modes are not found in the undoped  $\text{MgZr}_4(\text{PO}_4)_6$ . Moreover, the splitting of the Raman vibration band ranging from  $760$  to  $1300 \text{ cm}^{-1}$  [vibrational peaks at 846, 991, 1079, and  $1165 \text{ cm}^{-1}$ ] can be assigned to  $\text{Er}^{3+}$  ions photoluminescence emission stark levels under 514.5 nm laser excitation [38–42]. The  $(\text{PO}_4)^{3-}$  phonon energy is suppressed by  $\text{Er}^{3+}$  ions photoluminescence peaks due to their domination in photoluminescence intensity.

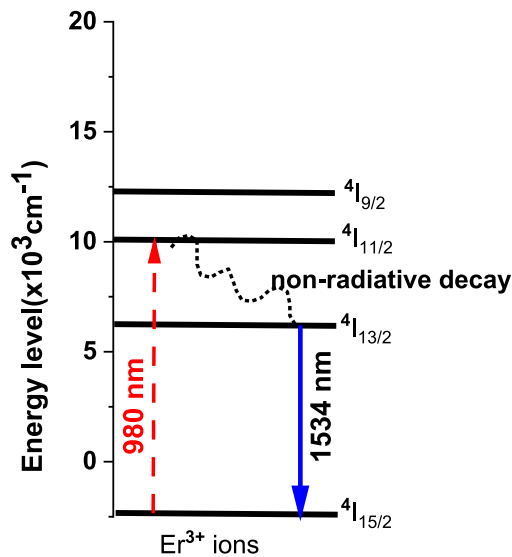


Fig. 5. Schematic energy level diagram of  $\text{Er}^{3+}$ , pumping with 980 nm excitation source and emission at 1534 nm wavelengths are indicated.

However, as the  $\text{Er}^{3+}$  ion concentration increased to 0.5 mol% [MZP3] and 1.00 mol% [MZP4], various Raman vibration peaks observed in samples MZP0, MZP1, and MZP2 at 406, 991, 1077, and 1627  $\text{cm}^{-1}$  disappeared to form a broad vibration band. The significant broadening and peak shift of the Raman spectra bands with overlapping weak peaks on samples MZP3 and MZP4 are mainly attributed to slight decreasing lattice strain and crystallite size [43] as shown in Table 1. This can be ascribed to optical phonon confinement in a small crystal size within nanometer range.

### 3.2.2. Photoluminescence (PL) properties

Fig. 5 illustrates a comparison of downconversion photoluminescence (PL) emission spectra and lifetime transients of Er doped  $\text{MgZr}_4(\text{PO}_4)_6$  nanophosphors with different concentrations of  $\text{Er}^{3+}$  ions under a 980 nm excitation of semiconductor diode laser measured at room temperature. The  $\text{Er}^{3+}$  ions PL emission measured from 1400 nm to 1700 nm at the near-infrared region arises from the characteristic band due to the  $^4\text{I}_{13/2}$  meta-stable state to the ground state,  $^4\text{I}_{15/2}$  state as shown in Fig. 5. The Er doped  $\text{MgZr}_4(\text{PO}_4)_6$  nanophosphors spectra shown in Fig. 6(a) reveal strong PL emission with a broad band peaked at 1533 nm wavelength. The PL spectra of samples MZP1 and MZP2 are almost identical with narrow band, however, the full width half maximum (FWHM) of sample MZP2 [FWHM = ~39 nm] is smaller than

sample MZP1 [FWHM = ~61 nm] as shown in Table 2. In contrast, as the  $\text{Er}^{3+}$  ion concentration increases to 0.75 (MZP3) and 1.00 mol% (MZP4) the PL intensity decreases with the increasing FWHM, respectively, which is attributed to concentration quenching effect.

Similarly, Fig. 6(b) shows the PL lifetime of  $\text{MgZr}_4(\text{PO}_4)_6$ :  $\text{Er}^{3+}$  concentration nanophosphors measured after exciting with a 980 nm excitation source at room temperature. The PL lifetime of these samples were monitored at 1533 nm ( $^4\text{I}_{13/2}$  transition) and then fitted with double exponential function. The average PL lifetime was calculated using the expression [44];

$$\tau_{av} = \frac{A_1\tau_1^2 + A_2\tau_2^2}{A_1\tau_1 + A_2\tau_2} \quad (5)$$

where  $A_1$  and  $A_2$  are pre-exponential factors,  $\tau_1$  and  $\tau_2$  are the rapid and slow lifetimes for the exponents. Table 2 illustrates average PL lifetime obtained from various  $\text{Er}^{3+}$  doping concentrations. The average lifetime obtained from equation (5) initially increases from 2.39 ms to 5.47 ms for samples MZP1 and MZP2 and then decreases very rapidly to 1.71 ms and 0.84 ms with increasing  $\text{Er}^{3+}$  doping concentrations. This can be ascribed to concentration quenching as well as change in local crystal field due to closely space  $\text{Er}^{3+}$  ion-ion interactions [42]. In addition, the appearance of second phase  $\text{Er}:\text{ZrO}(\text{PO}_4)_2$  identified from the XRD data as the  $\text{Er}^{3+}$  ion increases in MZP resulted in cluster formation of the  $\text{Er}^{3+}$  ions, which can potentially have contribute to decrease in PL intensity and lifetime [45].

## 4. Conclusions

In summary, results of structural, chemical and optical characterisation of  $\text{Er}^{3+}$  doped  $\text{MgZr}_4(\text{PO}_4)_6$  nanophosphor powders are presented with the aim of getting insights of crystal structure, crystallite size, lattice strain, crystal field interactions, and line broadening mechanisms. The selected area electron diffraction (SAED) patterns obtained from Transmission Electron Microscopy (TEM) reveal that the crystal structure of the host and  $\text{Er}^{3+}$  doped MZP remains as a single crystalline phase with the increase in concentration of  $\text{Er}^{3+}$  ions. This was further

Table 2

FWHM and average PL lifetime of the  $\text{MgZr}_4(\text{PO}_4)_6$ :  $x\text{Er}^{3+}$  nanophosphors at  $^4\text{I}_{13/2} \rightarrow ^4\text{I}_{15/2}$  transition for  $0.25 \leq x \leq 1$  mol% Er.

Sample ID	Er (mol%)	FWHM (nm)	Lifetime (ms)
MZP1	0.25	60.81	2.39
MZP2	0.50	38.90	5.47
MZP3	0.75	61.13	1.71
MZP4	1.00	64.65	0.84

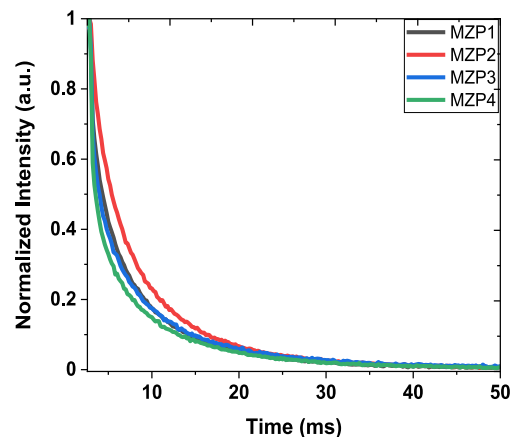
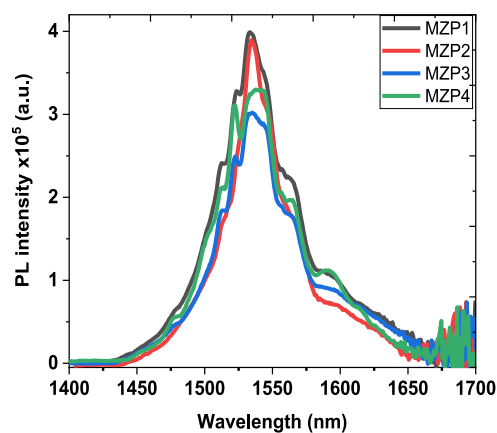


Fig. 6. (a)-(Left hand side) PL emission spectra of  $\text{MgZr}_4(\text{PO}_4)_6$ :  $x\text{Er}^{3+}$  nanophosphors with different concentrations of  $\text{Er}^{3+}$  ions intra-4f atomic transition  $^4\text{I}_{13/2} \rightarrow ^4\text{I}_{15/2}$  at room temperature using 980 nm excitation laser (b)-(Right hand side) Corresponding PL lifetime.

confirmed by XRD analysis. Scherrer equation and W-H analysis was used to obtain the crystallite size and lattice strain of the Er doped MZP nanophosphors as a function of concentration of Er dopant. The local structure influence of  $\text{Er}^{3+}$  ion concentrations on the PL properties of  $\text{MgZr}_4(\text{PO}_4)_6$  doped with  $\text{Er}^{3+}$  nanophosphors was also studied, which revealed strong intensity PL emission spectra at 1533 nm under a 980 nm pump wavelength. The FWHM value initially decreases from  $\sim 61$  nm to  $\sim 39$  nm for samples MPZ1 and MZP2 with corresponding PL lifetime of 2.4 ms and 5.5 ms. As the  $\text{Er}^{3+}$  doping concentration increases, the FWHM values of  $\sim 61$  and  $\sim 65$  nm were obtained for samples MZP3 and MZP4, nevertheless, PL lifetime of these samples decreased drastically to 1.7 ms and 0.8 ms, respectively. The decreasing in PL lifetime as the  $\text{Er}^{3+}$  doping concentration increases is attributed to concentration quenching effects and/or changes in local crystal field. The results obtained indicate that sample MPZ2 has a good PL properties, which is a suitable candidate with a huge potential for lighting, lasers and optical amplifiers around 1533 nm.

### Declaration of Competing Interest

The authors declare that they have no known competing financial interests or personal relationships that could have appeared to influence the work reported in this paper.

### Acknowledgement

The authors acknowledge the financial support from Engineering and Physical Sciences Research Council (EPSRC) for their financial support through the research Grants (EP/M015165/1, EP/T004711/1 and EP/M022854/1). This research was supported by the School of Chemical and Process Engineering internally by Dr Girish M. Kale. Thanks to Dr. Zabeada Aslam at Leeds Electron Microscopy and Spectroscopy (LEMAS) Centre, for the support in carrying out the TEM measurements.

### References

- [1] Y. Hong, H. Fan, B.o. Li, B.o. Guo, M. Liu, X. Zhang, Fabrication, biological effects, and medical applications of calcium phosphate nanoceramics, *Mater. Sci. Eng. R Rep.* 70 (3-6) (2010) 225–242.
- [2] R. Azarafa, A. Arab, A. Mehdiipoor, Impact Behavior of Ceramic- Metal Armour Composed of  $\text{Al}_2\text{O}_3$ -Nano SiC Composite, *Int. J. Adv. Des. Manuf. Technol.* 5 (2012) 83–87.
- [3] R. Bagga, V.G. Achanta, A. Goel, J.M.F. Ferreira, N.P. Singh, D.P. Singh, M. Falconieri, G. Sharma,  $\text{Dy}^{3+}$ -doped nano-glass ceramics comprising  $\text{NaAlSiO}_4$  and  $\text{NaY}_9\text{Si}_6\text{O}_{26}$  nanocrystals for white light generation, *Mater. Sci. Eng. B Solid-State Mater. Adv. Technol.* 178 (3) (2013) 218–224.
- [4] G.B. Nair, S.J. Dhoble, Highly enterprising calcium zirconium phosphate  $[\text{CaZr}_4(\text{PO}_4)_6 \cdot \text{Dy}^{3+}]$  phosphor for white light emission, *RSC Adv.* 5 (61) (2015) 49235–49247.
- [5] M. Ayvackl, A. Khatib, A. Ege, I. Sabikoglu, M. Henini, N. Can, Absorption and photoluminescence spectroscopy of  $\text{Er}^{3+}$ -doped  $\text{SrAl}_2\text{O}_4$  ceramic phosphors, *Philosophical Mag. Lett.* 92 (4) (2012) 194–201.
- [6] Z.-W. Zhang, L.u. Liu, X.-f. Zhang, J.-P. Zhang, W.-G. Zhang, D.-J. Wang, Preparation and investigation of  $\text{CaZr}_4(\text{PO}_4)_6$ :  $\text{Dy}^{3+}$  single-phase full-color phosphor, *Spectrochimica Acta Part A: Molecular and Biomolecular Spectroscopy* 137 (2015) 1–6.
- [7] E.R. Gobechiya, M.V. Sukhanov, V.I. Pet'kov, Y.K. Kabalov, Crystal structure of the double magnesium zirconium orthophosphate at temperatures of 298 and 1023 K, *Crystall. Rep.* 53 (1) (2008) 53–59.
- [8] D.E. Harrison, H.A. McKINSTRY, F.A. Hummel, High-temperature zirconium phosphates, *J. Am. Ceram. Soc.* 37 (6) (1954) 277–288.
- [9] M. Hirayama, N. Sonoyama, A. Yamada, R. Kanno, Structural investigation of  $\text{Eu}^{2+}$  emissions from alkaline earth zirconium phosphate, *J. Solid State Chem.* 182 (4) (2009) 730–735.
- [10] F. Chen, Q. Shen, J.M. Schoening, L. Zhang, Synthesis and Pressureless Sintering of Zirconium Phosphate Ceramics, *J. Am. Ceram. Soc.* 91 (10) (2008) 3173–3180.
- [11] R. Lin, Y. Ding, A Review on the synthesis and applications of mesostructured transition metal phosphates, *Materials* 6 (1) (2013) 217–243.
- [12] X. Lin, A. Feng, Z. Zhang, J. Zhao, VUV spectroscopic properties of rare-earth (RE=Eu, Tb and Dy)-doped  $\text{A}_2\text{Zr}(\text{PO}_4)_2$  (A=Li, Na and K) phosphates, *J. Rare Earths* 32 (10) (2014) 946–951.
- [13] G. Nataliai, K. Veronika, S. Petra, Influence of rare earth elements (REEs) on the structure and optical properties of lithium zirconium phosphate (LZP), *Cryst. Eng. Commun.* 22 (35) (2020) 5890–5899.

- [14] M. Adamu, G.M. Kale, Novel Sol-Gel Synthesis of  $\text{MgZr}_4\text{P}_6\text{O}_{24}$  composite solid electrolyte and newer insight into the  $\text{Mg}^{2+}$ -ion conducting properties using impedance spectroscopy, *J. Phys. Chem. C* 120 (2016) 17909–17915.
- [15] S. Liu, C. Zhou, Y. Wang, E. Yi, W. Wang, J. Kieffer, R.M. Laine, Processing combustion synthesized  $\text{Mg}_{0.5}\text{Zr}_2(\text{PO}_4)_3$  nanopowders to thin films as potential solid electrolytes, *Electrochem. Commun.* 116 (2020) 106753, <https://doi.org/10.1016/j.elecom.2020.106753>.
- [16] M. Hirayama, N. Sonoyama, A. Yamada, R. Kanno, Structural investigation of  $\text{Eu}^{2+}$  emissions from alkaline earthzirconium phosphate, *J. Solid State Chem.* 182 (4) (2009) 730–735.
- [17] M. Adamu, K.T. Jacob, G.M. Kale, Assessment of  $\text{MgZr}_4\text{P}_6\text{O}_{24}$  as a solid electrolyte for sensing Mg in molten non-ferrous alloys, *J. Electrochem. Soc.* 167 (2) (2020) 027532, <https://doi.org/10.1149/1945-7111/ab6556>.
- [18] M. Li, X. Li, W. Gong, P. Chen, B. Zhu, Tunability study on microstructure and electromagnetic properties of Ce-Doped  $\text{MgZr}_4\text{P}_6\text{O}_{24}$ , *J. Alloy. Compd.* 820 (2020), 153097.
- [19] I.G. Alhindawy, E.A. Elshehy, M.E. El-Khouly, Y.K. Abdel-Monem, M.S. Atrees, Fabrication of Mesoporous  $\text{NaZrP}$  Cation-Exchanger for U(VI) Ions Separation from Uranyl Leach Liquors, *Colloids Interfaces* 3 (4) (2019) 1–18, 61.
- [20] Y. Wang, G.e. Zhu, S. Xin, Q. Wang, Y. Li, Q. Wu, C. Wang, X. Wang, X. Ding, W. Geng, Recent development in rare earth doped phosphors for white light emitting diodes, *J. Rare Earths* 33 (1) (2015) 1–12.
- [21] V.I. Pet'kov, V.S. Kurzhkovskaya, A.I. Orlova, Synthesis and crystal chemical characteristics of the structure of  $\text{M} 0.5\text{Zr}_2(\text{PO}_4)_3$  phosphates, *Crystallogr. Rep.* 47 (2002) 736–743.
- [22] A. Kazakos-Kijowski, S. Komarneni, D. Agrawal, R. Roy, Synthesis, crystal data and thermal stability of magnesium zirconium phosphate  $[\text{MgZr}_4(\text{PO}_4)_6]$ , *Mater. Res. Bull.* 23 (8) (1988) 1177–1184.
- [23] E. Kumi-Barimah, D.E. Anagnostou, G. Jose, Phase changeable vanadium dioxide ( $\text{VO}_2$ ) thin films grown from vanadium pentoxide ( $\text{V}_2\text{O}_5$ ) using femtosecond pulsed laser deposition, *AIP Adv.* 10 (6) (2020) 065225, <https://doi.org/10.1063/5.0010157>.
- [24] P. Bindu, S. Thomas, Estimation of lattice strain in ZnO nanoparticles: X-ray peak profile analysis, *J. Theor. Appl. Phys.* 8 (4) (2014) 123–134.
- [25] D. Nath, F. Singh, R. Das, X-ray diffraction analysis by Williamson-Hall, Halder-Wagner and size-strain plot methods of CdSe nanoparticles- a comparative study, *Mater. Chem. and Phys.* 239 (2020) 122021, <https://doi.org/10.1016/j.matchemphys.2019.122021>.
- [26] M. Kurian, C. Kunjachan, Investigation of size dependency on lattice strain of nanoceria particles synthesised by wet chemical methods, *Int. Nano Lett.* 4 (4) (2014) 73–80.
- [27] R. Yogamalar, R. Srinivasan, A. Vinu, K. Ariga, A.C. Bose, X-ray peak broadening analysis in ZnO nanoparticles, *Solid State Comm.* 149 (43-44) (2009) 1919–1923.
- [28] R. Das, S. Sarkar, Determination of intrinsic strain in poly(vinylpyrrolidone)-capped silver nano-hexapod using X-ray diffraction technique, *Curr. Sci.* 109 (4) (2015) 775–778.
- [29] D. Balzar, H. Ledbetter, Voigt-function modelling in fourier analysis of size- and strain-broadened X-ray diffraction peaks, *J. Appl. Crystallogr.* 26 (1) (1993) 97–103.
- [30] I. Fejoo, M. Cabeza, P. Merino, G. Pena, M.C. Perez, S. Cruz, P. Rey, Estimation of crystallite and lattice strain in nano-sized TiC particle-reinforced 6005A aluminium alloy from X-ray diffraction line broadening, *Powder Technol.* 343 (2019) 19–28.
- [31] K.D. Litavosa, N.M. Podgornyykh, Raman spectroscopy of various phosphate minerals and occurrence of tuite in the Elga IIE iron meteorite, *J. Raman Spectrosc.* 48 (2017) 1518–1527.
- [32] M. Kazanci, P. Fratzl, K. Klaushofer, et al., Complementary Information on In Vitro Conversion of Amorphous (Precursor) Calcium Phosphate to Hydroxyapatite from Raman Microspectroscopy and Wide-Angle X-Ray Scattering, *Calcif Tissue Int.* 79, 354–359.
- [33] V. Raikwar, V. Bhatkar, S. Omanwar, Morphological and photoluminescence study of  $\text{NaSrB}_5\text{O}_9\text{:Tb}^{3+}$  nanocrystalline phosphor, *J. Asian Ceram. Soc.* 6 (4) (2018) 359–367.
- [34] J. Chandradass, B. Jun, D.-S. Bae, Effect of different fuels on the alumina-zirconia nanopowder synthesized by sol-gel autocombustion method, *J. Non-Cryst. Solids* 354 (26) (2008) 3085–3087.
- [35] N. Santha, V.N. Nayar, Vibrational spectra of  $\text{M}_3\text{Pb}(\text{P}_2\text{O}_7)_2$  ( $\text{M}^{\text{II}}=\text{Ni, Co}$ ), *J. Non-Crystall. Solids* 354 (26) (2008) 3085–3087.
- [36] S.N. Basahel, T.T. Ali, M. Mokhtar, K. Narasimharao, Influence of crystal structure of nanosized  $\text{ZrO}_2$  on photocatalytic degradation of methyl orange, *Nanoscale Res. Lett.* 10 (73) (2015) 1–13.
- [37] G.A.H. Mekhemer, Characterization of phosphate zirconia by XRD, Raman and IR spectroscopy, *Colloids Surf. A: Physicochem. Eng. Aspect* 141 (1998) 227–235.
- [38] D. Yan, P. Wu, S.P. Zhang, L. Liang, F. Yang, Y.L. Pei, S. Chen, Assignments of the Raman modes of monoclinic erbium oxide, *J. Appl. Phys.* 114 (19) (2013) 193502, <https://doi.org/10.1063/1.4831663>.
- [39] N. Tiwari, V. Dubey, Luminescence studies and infrared emission of erbium-doped calcium zirconate phosphor, *Luminescence* 31 (3) (2016) 837–842.
- [40] E. Kumi Barimah, M.W. Ziarko, N. Bamiedakis, I.H. White, R.V. Penty, G. Jose, Erbium-doped glass nanoparticle embedded polymer thin films using femtosecond pulsed laser deposition, *Opt. Mater. Exp.* 8 (7) (2018) 1997–2007.
- [41] K.S. Albarkaty, E. Kumi-Barimah, C. Craig, D. Hewak, G. Jose, J. Chandrapan, Erbium-doped chalcogenide glass thin film on silicon using femtosecond pulsed laser with different deposition temperatures, *Appl. Phys. A* 125 (2019) 1–8.
- [42] Eric Kumi Barimah, Sri Rahayu, Marcin W. Ziarko, Nikolaos Bamiedakis, Ian H. White, Richard V. Penty, Girish M. Kale, Gin Jose, Erbium-Doped

- Nanoparticle–Polymer Composite Thin Films for Photonic Applications: Structural and Optical Properties, ACS Omega 5 (16) (2020) 9224–9232.
- [43] M. Yang, D. Huang, P. Hao, F. Zhang, X. Hou, X. Wang, Study of the Raman peak shift and the linewidth of light-emitting porous silicon, J. Appl. Phys. 75 (1) (1994) 651–653.
- [44] I.E. Kolesnikov, A.A. Kalinichev, M.A. Kurochkin, E.V. Golyeva, A.S. Terentyeva, E. Y. Kolesnikov, E. Lähderanta, Structural, luminescence and thermometric properties of nanocrystalline  $\text{YVO}_4:\text{Dy}^{3+}$  temperature and concentration series, Sci. Rep. 9 (2019) 2043.
- [45] C.R. Kesavulu, H.J. Kim, S.W. Lee, J. Kaewkhao, N. Wantana, S. Kothan, S. Kaewjaeng, Influence of  $\text{Er}^{3+}$  ion concentration on optical and photoluminescence properties of  $\text{Er}^{3+}$ -doped gadolinium-calcium silica borate glasses, J. Alloy. Compd. 683 (2016) 590–598.